Contributions to Mineralogy and Petrology (2024) 179:3
https://doi.org/10.1007/s00410-023-02084-y

ORIGINAL PAPER

# The Fe(Ni)–C–N-phase diagram at 10 GPa—implications for nitrogen and carbon storage in the deep mantle

**Paul Pangritz[1] · Arno Rohrbach[1] · Christian Vollmer[1] · Jasper Berndt[1] · Susanne Müller[1,2] · Dražen Radić[3] · Simon Basten[1] · Stephan Klemme[1]**

Received: 28 July 2023 / Accepted: 16 November 2023 / Published online: 16 December 2023


## Abstract

Nitrogen is the most abundant element in the Earth's atmosphere, yet its geochemical behavior and distribution among the various reservoirs (atmosphere, crust, mantle, and core) remain poorly understood. Although estimates of N and C fluxes in the mantle vary, there is a consensus regarding the disparity between input and output, leading to an increase in N and C contents in the mantle. The low solubility of N in mantle minerals raises questions about possible N or C storage in the mantle. Evidence suggests that Fe–N–C phases, such as $Fe_3C$, $Fe_7C_3$, ε-$Fe_3N$, metals, and non-stoichiometric carbonitrides, may be accessory phases at mantle pressure and temperature conditions, and thus potential hosts of C and N in the deep mantle. To investigate the phase relations and melting behavior in the (Fe,Ni)–N–C system, 19 experiments were conducted with varying starting compositions at 10 GPa and 1000–1400 °C. The results indicate that carbides, nitrides, carbonitrides, nitrocarbides, Fe(Ni)-metal, Fe-oxides, and diamond are stable at deep upper mantle pressure conditions. However, the compositions of naturally occurring nitrocarbides with high C and N contents, as found in diamond inclusions, could not be reproduced in the experiments. The significant incorporation of Ni in the experimental phases, which is also not observed in natural carbonitrides and nitrocarbides, suggests their formation in Ni-poor regimes. The solidus temperatures of the N- and C-rich systems are well below the adiabatic temperatures of the surrounding mantle. Therefore, it is hypothesized that cold regions in subduction zones, such as within or at the edge of a C- and N-rich subducted plate, are the likely formation environment for solid Fe–C–N phases.

**Keywords** Nitrides · Carbides · High-pressure · Diamond inclusions · Phase diagram

Communicated by Dante Canil.

✉ Paul Pangritz
paul.pangritz@uni-muenster.de

Arno Rohrbach
arno.rohrbach@uni-muenster.de

Christian Vollmer
christian.vollmer@uni-muenster.de

Jasper Berndt
jberndt@uni-muenster.de

Susanne Müller
Susanne.muller@esrf.fr

Dražen Radić
d_radi01@uni-muenster.de

Simon Basten
bastensim@gmail.com

Stephan Klemme
stephan.klemme@uni-muenster.de

[1] Institut für Mineralogie, Universität Münster, Corrensstrasse 24, 48149 Münster, Germany

[2] European Synchrotron Radiation Facility (ESRF) 71, 38043 Grenoble, France

[3] Institut für Materialphysik, Universität Münster, Wilhelm-Klemm-Str. 10, 48149 Münster, Germany

## Introduction

Nitrogen (N) and carbon (C) are highly volatile elements that are commonly associated with the Earth's atmosphere and crust, and hence, have a profound impact on the habitability and evolution of the biosphere. Understanding the abundance and cycling of these elements on Earth is, therefore, an important subject in modern geochemistry (Dasgupta and Hirschmann 2010; Halama et al. 2014; Halama and Bebout 2021; Johnson and Goldblatt 2015; Marty 2012).

Nitrogen gas is relatively unreactive due to the strong N–N bonding, and hence most of the N partitions primarily into the atmosphere (White 2013). However, although the atmosphere consists of approximately 78% $N_2$, the Earth's mantle is the primary N reservoir in terms of mass, the latter of which contains about 57% of the global N, followed by the atmosphere (27%) and the continental crust (14%) (Goldblatt et al. 2009; Ni and Keppler 2013; Palya et al. 2011). Note that the uncertainties of N concentrations in the mantle vary significantly through different studies but the overall trend of the mantle to host the majority of global N is accepted. However, the N concentrations in these reservoirs have changed significantly over geological timescales due to the coupling of biological and geological N-cycles (Bebout et al. 2013). Ammonium ($NH^{4+}$) can be incorporated in K-rich silicates, such as clay minerals, mica, or feldspars (Yang et al. 2022), where $K^+$ is substituted by $NH_4^+$ (Jackson et al. 2021b; White 2013), and this is an effective mechanism that transfers N from the biological into the geological cycle. The subsequent sedimentation and subduction of N-bearing silicates results in the development of N-rich fluids and further N subduction into the deep upper or even the lower mantle (Fukuyama et al. 2023). Although different N fluxes between reservoirs have been calculated in previous studies, there is general agreement that N flux into the Earth's mantle is significantly higher than the N flux out of the mantle (e.g., Halama et al. 2014; Sano et al. 2001).

Carbon also plays a key role in the habitability of Earth as it is the main constituent of living organisms, it affects the global climate, and also tectonics in the crust (Fischer et al. 2020). Similar to N, C cycling is also unbalanced in terms of flux into and flux out of the mantle (Dasgupta 2013; Dasgupta and Hirschmann 2010; Halama and Bebout 2021), and hence a C-rich reservoir has been proposed which is not influenced by oceanic volcanism (Dasgupta and Walker 2008). Most estimates of C concentration in the bulk silicate Earth (BSE) are in a range of 100–260 ppm (Hirschmann 2018; Marty et al. 2020; McDonough and Sun 1995), while estimations of average mantle C are in the same order of magnitude, i.e., 20–300 ppm; (Javoy and Pineau 1991; Marty and Tolstikhin 1998; Saal et al. 2002; Trull et al. 1993; Zhang and Zindler 1993) increasing with depth to 117–669 ppm (< 200 km; Aiuppa et al. 2021). Due to the low solubility of C in silicate mantle minerals, such as olivine, enstatite, diopside, pyrope, and spinel, (Keppler et al. 2003; Shcheka et al. 2006), C in the mantle is probably stored mainly in accessory mineral phases such as Ca- and Mg-carbonates in the upper mantle and as diamond in the more reduced deeper mantle (Bulanova and Zayakina 1991; Dasgupta and Hirschmann 2010; Rohrbach and Schmidt 2011; Stagno et al. 2013) depending on the given P–T conditions. Furthermore, C can be stable as $Fe_3C$ or $Fe_7C_3$ in ultra-reduced mantle domains (Dasgupta and Hirschmann 2010; Frost and McCammon 2008; Lord et al. 2009; Rohrbach et al. 2014; Sokol et al. 2017b).

The imbalance between the flux into and flux out of the mantleof both C and N, and the low solubility of both elements in silicate mantle minerals (Keppler et al. 2003, 2022; Li et al. 2016; Shcheka et al. 2006; Yokochi et al. 2009; Yoshioka et al. 2018), leads consequently to a deep hidden reservoir of C- and N-bearing phases that may be progressively enlarged by subduction over geologic time. Natural evidence for possible N and C storage in the deep Earth are Fe–N–C phases that have been found as inclusions in sublithospheric diamonds (Kaminsky and Wirth 2011, 2017). While all natural diamonds contain N as impurities and are classified based on their N contents into Type I (> 1-2 ppm) and Type II (< 1–2 ppm) (Mikhail and Howell 2016), which are a result of structural defects (Ashfold et al. 2020), mineral inclusions in super-deep diamonds from Rio Soriso (Brazil) show that C and N can also be stored in the Earth's deep mantle as carbides, carbonitrides, and nitrides (Kaminsky and Wirth 2017). Diamonds from the Juina region in Brazil also contain inclusions of iron-carbides with 7.3–9.1 at% N coexisting with graphite, magnetite, and native iron (Kaminsky and Wirth 2011). Other diamonds from the same region have inclusions of microcrystalline, polymineralic aggregates with nitrocohenite $Fe_3(C,N)$, nitrochalypite $Fe_7(C,N)_3$, or $Fe_2(C,N)$, and nitroyarlongite $Fe_9(C,N)_4$ (Kaminsky et al. 2015). Moreover, trigonal $Fe_3(N_{0,8}C_{0,2})_{1,38}$, a synthetic carbonitride that has previously been synthesized in the laboratory (Leineweber et al. 2001), has also been found as a natural inclusion in diamond and this phase contains 17.5 at% N and has a N/(C + N) ratio of 0.74 (Kaminsky et al. 2015). Therefore, there is profound evidence from natural samples that iron carbides, nitrocarbide/carbonitride, and metal melts may be stable phases at mantle conditions.

In this study, we investigate the stability field and a possible formation regime of Fe–N–C inclusions in diamonds, by conducting experiments at 10 GPa and temperatures between 1000 and 1400 °C.

## Experimental and analytical methods

### Starting materials

Starting materials were prepared by mixing high-purity $Fe_{2-4}N$ iron nitride with pure graphite, Ni-metal, and Fe-metal (Alfa Aesar GmbH, Germany). Fe-nitride starting powder was previously analyzed by X-ray powder diffraction and consists of pure $Fe_2N$, $Fe_4N$, and $Fe_{2-3}N$. To characterize the exact N content of the $Fe_{2-4}N$ starting material powder, we conducted an experiment (PPMA5.2) with only Alfa Aesar $Fe_{2-4}N$, as further calculations of starting materials required accurate knowledge of N content in the powder. Nitrogen content in the mixtures (Table 1) was controlled by recalculating starting compositions and adding metallic Fe to the $Fe_{2-4}N$ powder, while C was varied by adding pure graphite. All starting materials were stored in a desiccator to prevent oxidation of metal ingredients. Starting compositions were homogenized using an agate mortar with acetone for at least 20 min. Leftover acetone was evaporated by storing the mixture under a red light lamp for ~ 15 min. Although the starting materials were stored in a desiccator, a small fraction of iron reacted with oxygen and produced small amounts (~ 1–3%) of wüstite.

### High-pressure experiments

All experiments were performed in a 1000 t walker-type multi-anvil apparatus at the Institute of Mineralogy, University of Münster. We used a 14/8 assembly that consists of Cr-doped MgO octahedra (14 mm edge length; Ceramic substrates), stepped $LaCrO_3$ (Hamasho Corporation, Japan) furnaces, and pyrophyllite (Wonderstone Ltd, South Africa) gaskets. The assembly was calibrated using solid-state mineral phase transformations as described by Wijbrans et al. (2016). Polycrystalline crushable $Al_2O_3$ capsules (TKF Technische Keramik Frömgen GmbH, Germany) were used for 1000 °C experiments, while high-temperature runs (1400 °C) were performed in MgO single crystal capsules (Korth Kristalle GmbH, Germany). The starting material powders were carefully pressed into the capsules. Most experiments were run with two capsules stacked on top of each other centered in the hot zone of the furnace.

The temperatures were measured using W–Re (type-C) thermocouples (WHS Sondermetalle GmbH & Co. KG) placed directly in contact with the top of the capsule. All experiments were heated to about 900 °C as quickly as possible, i.e., within a few seconds, by closing the current circuit at a previously adjusted operation power. Once the experiment stabilized after a few minutes, it was heated more slowly at about 100°/min to the target temperature. During all experiments, temperature was controlled by a Eurotherm 2404 (Schneider Electric GmbH, Germany) controller. Temperature variations were generally less than ± 3 °C during all runs. Samples were quenched by turning off the power supply resulting in a temperature decrease to below 500 °C within 1 s.

**Table 1** Experimental conditions and starting material compositions

| Run | Temp/°C | Time/h | Starting material composition/at% | | | |
|---|---|---|---|---|---|---|
| | | | C | N | Ni | Fe |
| PPMA5.1/MA448 | 1400 | 48 | – | 22.2 | – | 77.8 |
| PPMA5.2/MA448 | 1400 | 48 | – | 23.3 | – | 76.7 |
| PPMA7.1/MA459 | 1000 | 48 | 10.3 | 20.9 | – | 68.8 |
| PPMA7.2/MA459 | 1000 | 48 | – | 20.0 | – | 80.0 |
| PPMA9.1/MA468 | 1000 | 48 | – | 16.5 | – | 83.5 |
| PPMA9.2/MA468 | 1000 | 48 | – | 18.0 | – | 82.0 |
| PPMA10/MA471 | 1400 | 3 | – | 18.0 | – | 82.0 |
| PPMA12MA473 | 1400 | 3 | 8.2 | 5.2 | – | 86.6 |
| PPMA13/MA474 | 1000 | 48 | 8.2 | 5.2 | – | 86.6 |
| PPMA15.1/MA485 | 1000 | 25 | 9.7 | 11.7 | – | 78.7 |
| PPMA15.2/MA485 | 1000 | 25 | – | 10.8 | – | 89.2 |
| SIM1.1/MA481 | 1000 | 24 | 14.9 | 10.0 | 15.0 | 60.1 |
| SIM1.2/MA481 | 1000 | 24 | 7.6 | 7.5 | 42.5 | 42.4 |
| SIM2.1/MA487 | 1000 | 24 | 25.0 | 10.0 | 6.6 | 58.4 |
| SIM2.2/MA487 | 1000 | 24 | – | 10.0 | 45.0 | 45.0 |
| SUS1.1*/MA483 | 1000 | 24 | 13.5 | – | 13.9 | 72.7 |
| SUS1.2*/MA483 | 1000 | 24 | 28.1 | – | 4.6 | 67.7 |
| SUS2.1*/MA486 | 1000 | 24 | 12.5 | 10.5 | – | 76.0 |
| SUS2.2*/MA486 | 1000 | 24 | 10.0 | 6.0 | – | 83.0 |

## Analytical methods

The entire octahedron was mounted in two-component epoxy resin to investigate possible leaks of the capsules or deformation of the whole setup. Mounts were polished for scanning electron microscopy (SEM) and electron probe microanalysis (EPMA) using 0.25 µm polycrystalline diamond spray and ethanol. Polished samples were precleaned in an ultrasonic bath with petroleum ether before cleaning them in a plasma cleaner using an Ar-plasma. Cleaned samples were coated with a 10 nm iridium layer and stored in a desiccator until analysis. Textural observations were done with a JEOL JSM 6510LA SEM (tungsten filament) using 20 kV acceleration voltage. For chemical analysis, a JEOL JXA 8530F Electron Microprobe was used (e.g. (Flemetakis et al. 2020). As reference materials, "Astimex" BN, nickel- and iron-metal, and "Plano" $Fe_3C$ were measured. Samples were measured at 15 kV acceleration voltage and 15 nA beam current. For the N measurements, the position of the peak and the background were calibrated by several measurements on a boron nitride (BN) standard. Quantitative analyses were performed using a defocused electron beam of 5–10 µm diameter.

To reduce carbon contamination in the sample chamber, a liquid-N cold trap was used instead of an N-containing air plasma, as the latter can form a Fe–N coating on the surface (Ertl et al. 1979), which would lead to errors in the N measurements. However, the build-up of carbon contamination cannot be prevented. Thus, all analyses were corrected for C blank signal which has been determined by a linear fit of C Kα count rates on a set of pure Fe- and C-references steels vs published C-contents. All EPMA parameters, including standards and carbon standard blank runs, are given in Table 3 and 4 in the Supplementary Information. The matrix corrections were made according to the $\varphi(\rho z)$ procedure outlined by (Armstrong 1991).

In addition, an electron-transparent lamella was prepared at the grain boundary between two phases from sample PPMA15.1 using a Zeiss CrossBeam 340 Focused Ion Beam (FIB)–SEM system at the Münster Nanofabrication Facility (MNF). Lamella extraction was performed using 30 kV $Ga^+$ ions applying standard FIB protocols. The final lamella was thinned to electron transparency with progressively lower beam energies down to 2 kV to reduce amorphization layers. Transmission Electron Microscopy (TEM) investigations were performed on an image-corrected ThermoFisher Scientific TITAN Themis G3 60–300 at the University of Münster, operated with an acceleration voltage of 300 kV. The TEM is equipped with a high-brightness field emission gun (X-FEG), a Wien-filter-type monochromator, a four-quadrant silicon-drift EDX detector (SuperX technology), a Fischione Model 3000 high-angle annular darkfield (HAADF) detector for Z-contrast imaging, a fast CMOS camera (Ceta 4 k x 4 k), and a post-column Gatan Quantum 965 electron energy loss spectrometer. We analyzed the samples by conventional brightfield (BF), high-resolution (HR) imaging, and selected area electron diffraction (SAED) to document the mineralogy, texture, and crystallography of studied samples. Chemical quantification was carried out by energy-dispersive X-ray (EDX) and electron energy loss spectroscopy (EELS) in scanning TEM (STEM) mode.

## Results

### Textural observations

The results of all experiments are listed in Table 2. All phases from successful experiments show intact capsules without leakage or diffusion of elements into the capsule material. All phases are not zoned and are chemically homogenous within the analytical uncertainties. Variations in backscatter electron (BSE) contrast are observed in several experiments, although the EPMA analyses show that these phases are chemically identical (sample PPMA#005; Fig. 1 in Supplementary Information). This effect is interpreted as electron channel contrast that is known to depend on crystal orientation (Weidner and Biermann 2015). Smaller angles between the primary electron beam and the crystal lattice lead to smaller backscattered electron coefficients, since the primary electrons that penetrate deeper into the sample material are scattered further, and thus fewer electrons can leave the sample, resulting in an overall patchy texture (Weidner and Biermann 2015). As all single-phase experiments at the Fe–N site of the pseudoternary diagram reveal the same composition before and after the experiment, we see no indication of N loss during the runs. Conversely, phase compositions shown in Fig. 5 appear rather N enriched relative to the respective starting composition, because minor amounts of FeO formed in all experiments (see Fig. 5). Since metal melts do not quench to homogeneous phases (e.g. Kurz and Fisher 1998), textural observations were used to determine whether the phases were molten or solid at high P and T. The molten experiment with high carbon content (PPMA12) unmixes upon cooling into a metal and a carbide phase, often with a finely lamellar 'spinifex-like' texture (Fig. 1c). Sub-solidus experiments, on the other hand, show either a single phase with a slightly patchy texture (Fig. 2 in Sup.) or, in the case of multiphase experiments, granular textures with well-developed 120° equilibrium grain boundaries (Fig. 1d). The solidus at 10 GPa pressure in the pure ε-$Fe_xN$ system is > 1400 °C, since no quench textures were observed in the 1400 °C experiments. However, the Fe–N–C phases were fully molten at 1400 °C (at 10 GPa pressure) but showed no evidence of melting at 1000 °C.

**Table 2** Experimental run conditions and average phase compositions measured by EPMA

| Experiment | T | Time | n | Wt% | | | | | At% | | | | | | |
|---|---|---|---|---|---|---|---|---|---|---|---|---|---|---|---|
| | (°C) | (h) | | C | N | Ni | Fe | Total | C | N | Ni | Fe | Total | N/[C+N] | Phase |
| PPMA5.1 MA448 | **1400** | **48** | 33 | n.d | 6.86±0.34 | n.a | 93.56±0.79 | 100.4 | n.d | 22.63±0.83 | n.a | 77.37±0.83 | 100 | 1 | Nitride |
| PPMA5.2 MA448 | **1400** | **48** | 17 | n.d | 7.11±0.27 | n.a | 93.63±0.40 | 100.7 | n.d | 23.25±0.64 | n.a | 76.75±0.64 | 100 | 1 | Nitride |
| PPMA7.1 MA459 | **1000** | **48** | 3 | 8.04±0.44 | 0.48±0.09 | n.a | 91.75±0.91 | 100.3 | 28.52±1.04 | 1.47±0.30 | n.a | 70.01±0.74 | 100 | 0.05 | Carbide + Diamond |
| | | | 7 | 1.74±0.23 | 6.64±0.26 | n.a | 91.89±0.55 | 100.3 | 6.41±0.76 | 20.93±0.57 | n.a | 72.66±1.13 | 100 | 0.77 | Carbonitride |
| PPMA7.2 MA459 | **1000** | **48** | 6 | 0.24±0.10 | 5.68±0.21 | n.a | 94.44±0.62 | 100.4 | 0.93±0.40 | 19.16±0.58 | n.a | 79.92±0.59 | 100 | 0.95 | Nitride |
| PPMA9.1 MA468 | **1000** | **48** | 23 | n.d | 4.67±0.37 | n.a | 96.18±0.51 | 100.8 | n.d | 16.21±1.08 | n.a | 83.79±1.08 | 100 | 1 | Nitride |
| PPMA9.2 MA468 | **1000** | **48** | 19 | n.d | 5.24±0.51 | n.a | 95.91±0.46 | 101.2 | n.d | 17.9±0.37 | n.a | 82.1±1.37 | 100 | 1 | Nitride |
| PPMA10 MA471 | **1400** | **3** | 5 | n.d | 5.38±0.42 | n.a | 95.50±0.19 | 100.9 | n.d | 18.33±1.19 | n.a | 81.67±1.19 | 100 | 1 | Nitride |
| PPMA12 MA473 | **1400** | **3** | 7 | 6.07±0.15 | n.d | n.a | 92.46±1.27 | 98.5 | 23.36±0.53 | n.d | n.a | 76.58±0.64 | 100 | 0 | Carbide |
| | | | 7 | 0.22±0.08 | 1.76±0.23 | n.a | 96.39±0.49 | 98.4 | 0.97±0.35 | 6.70±0.84 | n.a | 92.32±0.61 | 100 | 0.87 | Nitride/Metal |
| PPMA13 MA474 | **1000** | **48** | 10 | 6.31±0.24 | n.d | n.a | 92.94±0.32 | 99.3 | 23.99±0.72 | n.d | n.a | 75.96±0.65 | 100 | 0 | Carbide |
| | | | 9 | 0.43±0.22 | 1.59±0.29 | n.a | 97.45±0.48 | 99.5 | 1.90±0.95 | 6.00±1.07 | n.a | 92.2±0.93 | 100 | 0.76 | Metal |
| PPMA15.1 MA458 | **1000** | **25** | 19 | 0.10±0.10 | 4.96±0.38 | n.a | 94.32±0.65 | 100.3 | 3.91±0.38 | 16.66±1.07 | n.a | 79.42±1.04 | 100 | 0.81 | Carbonitride |
| | | | 9 | 5.90±0.32 | 0.13±0.23 | n.a | 94.29±0.39 | 100.3 | 22.44±1.0 | 0.41±0.74 | n.a | 77.15±1.10 | 100 | 0.02 | Carbide |
| PPMA15.2 MA458 | **1000** | **25** | 8 | 0.42±0.09 | 4.05±0.18 | n.a | 96.16±0.45 | 100.6 | 1.72±0.36 | 14.13±0.54 | n.a | 84.14±0.50 | 100 | 0.89 | Nitride |
| | | | 5 | 0.29±0.19 | 2.30±0.32 | n.a | 97.96±0.31 | 100.6 | 1.22±0.81 | 8.45±1.06 | n.a | 90.31±1.44 | 100 | 0.87 | Metal |
| SIM1.1 MA481 | **1000** | **24** | 15 | 0.91±0.12 | 2.64±0.28 | 40.93±0.36 | 55.32±0.74 | 99.8 | 3.89±0.51 | 9.67±0.95 | 35.71±0.60 | 50.73±0.64 | 100 | 0.71 | Nitride |
| | | | 12 | 0.46±0.15 | 1.01±0.26 | 52.15±1.41 | 46.49±0.74 | 100.1 | 2.08±0.68 | 3.95±0.98 | 48.51±0.99 | 45.46±1.69 | 100 | 0.65 | Metal |
| SIM1.2 MA481 | **1000** | **24** | 16 | 1.44±0.12 | 3.89±0.29 | 20.52±1.84 | 74.16±1.70 | 100 | 5.77±0.44 | 13.39±0.84 | 16.85±1.58 | 63.90±1.42 | 100 | 0.70 | Nitride |
| | | | 5 | 5.45±0.20 | n.d. | 18.44±0.75 | 75.94±0.90 | 100 | 21.20±0.56 | n.d. | 14.68±0.75 | 63.53±0.70 | 100 | 0.03 | Carbide |
| SIM2.1 MA487 | **1000** | **24** | 11 | 1.56±0.15 | 5.34±0.38 | 11.47±0.61 | 81.34±0.78 | 99.7 | 6.02±0.46 | 17.61±0.93 | 9.04±0.59 | 67.33±0.95 | 100 | 0.75 | Nitride |
| | | | 7 | 7.05±0.37 | n.d. | 8.14±0.31 | 84.47±0.93 | 100 | 25.98±1.10 | n.d. | 6.14±0.32 | 66.94±0.91 | 100 | 0.03 | Carbide |
| SIM2.2 MA487 | **1000** | **24** | 4 | n.d. | 0.90±0.33 | 56.88±0.57 | 41.99±0.33 | 99.9 | n.d. | 3.59±1.29 | 54.06±0.87 | 41.96±0.61 | 100 | 0.90 | Metal |
| | | | 9 | 0.24±0.16 | 5.08±0.44 | 32.91±0.72 | 61.52±0.99 | 99.8 | 0.99±0.64 | 17.74±1.34 | 27.40±0.44 | 53.87±1.48 | 100 | 0.95 | Nitride |
| SUS1.1 MA483 | **1000** | **24** | 19 | 6.71±0.28 | n.a | 5.01±1.20 | 88.07±1.69 | 100.1 | 25.12±0.84 | n.a | 3.84±0.96 | 70.86±1.05 | 100 | 0 | Carbide |
| | | | 13 | 0.86±0.07 | n.a | 18.39±1.80 | 77.75±3.94 | 99.4 | 3.99±0.38 | n.a | 17.37±1.70 | 77.18±2.64 | 100 | 0 | Metal |
| SUS1.2 MA483 | **1000** | **24** | 19 | 6.67±0.35 | n.a | 5.05±0.79 | 88.29±1.12 | 100.5 | 24.92±0.92 | n.a | 3.86±0.61 | 70.96±1.06 | 100 | 0 | Carbide |
| SUS2.1 MA486 | **1000** | **24** | 16 | 1.75±0.22 | 5.43±0.46 | n.a | 90.44±2.14 | 99.4 | 6.72±0.72 | 17.85±1.26 | n.a | 74.58±1.78 | 100 | 0.73 | Carbonitride |
| | | | 4 | 6.62±0.33 | 0.09±0.05 | n.a | 92.96±0.80 | 100.2 | 24.73±0.91 | 0.29±0.16 | n.a | 74.65±1.09 | 100 | 0.01 | Carbide |
| | | | 7 | 8.31±0.27 | 0.16±0.10 | n.a | 91.63±0.81 | 100.4 | 29.46±0.80 | 0.48±0.29 | n.a | 69.87±0.80 | 100 | 0.02 | Carbide |

**Table 2** (continued)

| Experiment | T | Time | n | Wt% | | | | | At% | | | | | | |
|---|---|---|---|---|---|---|---|---|---|---|---|---|---|---|---|
| | (°C) | (h) | | C | N | Ni | Fe | Total | C | N | Ni | Fe | Total | N/[C + N] | Phase |
| SUS2.2 | **1000** | **24** | 21 | 1.27 ± 0.11 | 4.26 ± 0.12 | n.a | 92.49 ± 0.1.46 | 99.2 | 5.07 ± 0.43 | 14.61 ± 0.51 | n.a | 79.51 ± 1.89 | 100 | 0.74 | Carbonitride |
| MA486 | | | 7 | 6.56 ± 0.22 | 0.06 ± 0.06 | n.a | 93.05 ± 1.72 | 100 | 24.61 ± 0.68 | 0.20 ± 0.18 | n.a | 75.02 ± 0.79 | 100 | 0.01 | Carbide |

All experiments were run at a pressure of 10 GPa, *T* temperature, *t* time/hours, *At%* atom percent, *Wt%* weight percent, *n* = number of analyses with EPMA, *n.a.* not analyzed, *n.d.* not detected

## Structural observations

TEM investigations reveal additional information about structural and chemical properties and sub-µm textures of the respective phases. Figure 2a shows an overview of the FIB lamella with two different phases ($Fe_3C$ and "carbonitride") using bright field (BF) imaging. The carbonitride consists of at least three grains in different orientations clearly visible by strong and variable diffraction contrast with abundant dislocations (Fig. 2b) which are common in high-pressure experiments (e.g. Rubie 1999). The dislocations are also visible by HR imaging, but all phases have in general well-developed crystal lattices (Fig. 2c). Dislocations are a common phenomenon in HP experimental run products and also decorate grain boundaries between different carbonitride grains and to the carbide. Such dislocations have also been documented in carbonitride grains in diamond inclusions (Kaminsky and Wirth 2011). EELS as well as EDX analyses of chemical compositions were acquired from both $Fe_3C$ and the carbonitride. EELS measurements reveal Fe/C = 3 with very little N for cohenite also visible in extracted spectra (Fig. 2d), while EDX spectra show higher N contents with N/(N + C) ~ 0.19. The absolute N content of the carbide is ~ 1 wt.% by EDX, which is the reason why we do not see a strong N–K edge in EEL spectra. For the carbonitride, EDX analyses give N/(N + C) ~ 0.74, which is within the range of the composition of synthetic carbonitride described in previous work of N/(N + C) ~ 0.8 (Leineweber et al 2001). We did not quantify Fe/(N,C) ratios, because, due to matrix effects, light elements, such as N and C, in relation to Fe, are strongly underrepresented in EDX measurements, because theoretical k-factors are not reliable in samples of unknown thickness and high-Z (i.e., mainly Fe) matrix. In general, our TEM analyses confirm results by EMPA (Tab. 2). However, N contents are apparently more variable on a sub-µm scale than observed by electron microprobe.

Subsequently, both phases were also analyzed by selected area electron diffraction (SAED) analyses. SAED patterns of the two phases can be indexed to clearly distinct zone axes of cohenite ($Fe_3C$) (Fig. 2e) and a non-stoichiometric carbonitride ($Fe_3(N,C)_{1.395}$) known from synthesis experiments (Leineweber et al. 2001) and as diamond inclusions (Kaminsky and Wirth 2011) (Fig. 2f). For the $Fe_3C$ phase, measured *d* values of 0.51 nm and 0.21 nm fit well to (100) and (031) planes, respectively, of the cohenite structure (Fig. 2e), while for the second phase, measured *d* values of 0.44 nm and 0.23 nm correspond to (001) and (2–10) planes, respectively, of the carbonitride structure (Fig. 2f).

## The ε-$Fe_3N$ phase

The ε-$Fe_xN$ phase is often referred to as ε-$Fe_3N$, indicating a stoichiometric phase with a constant Fe–N ratio, such as

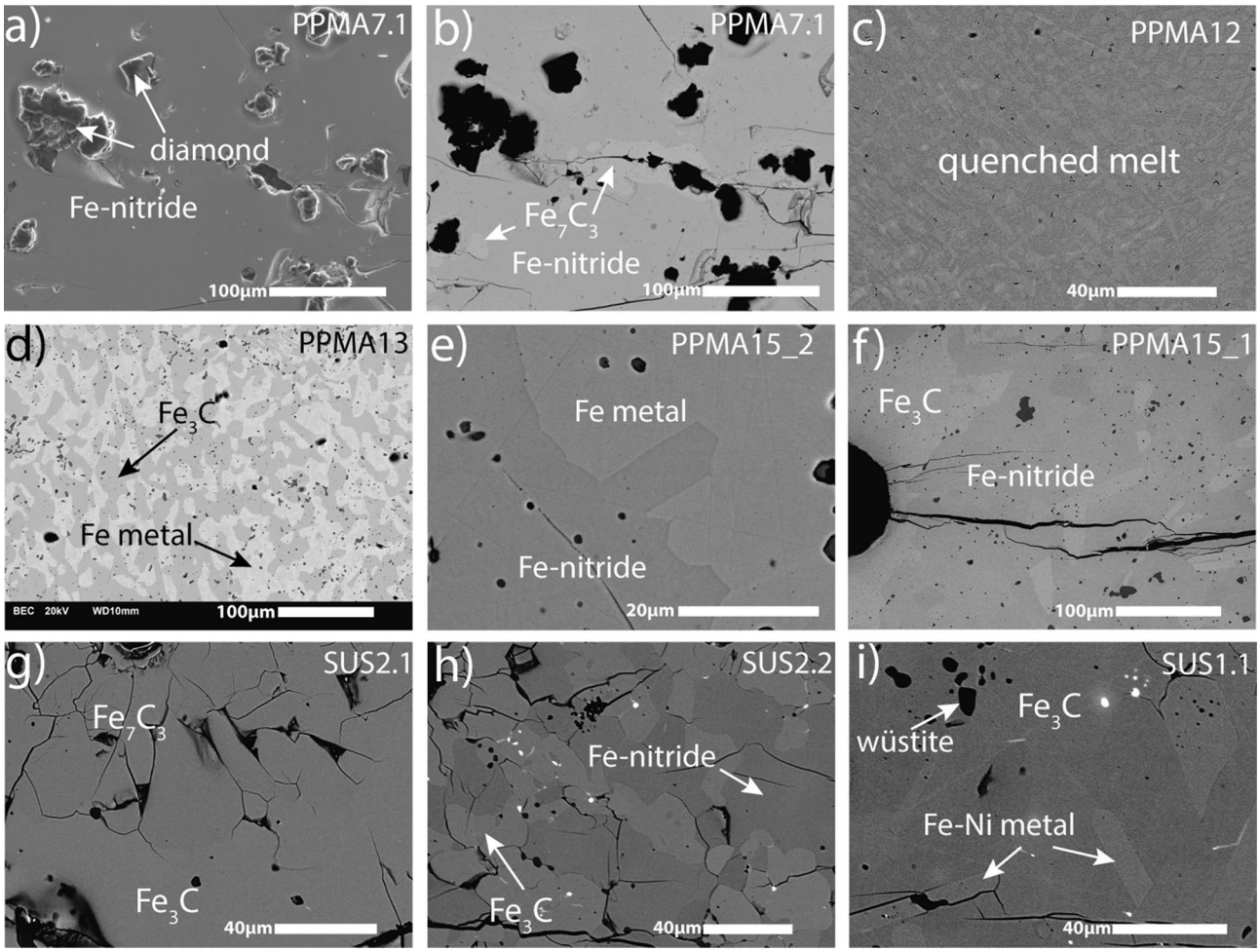


**Fig. 1** SEM images of subsolidus (except **c**) run products showing all coexisting phases. All experimental results contain wustite grains indicating a redox state near the Fe–FeO buffer system. **a** Secondary electron image of Sample PPMA#007.1 with diamond, carbonitride ($Fe_9(N_{0.64}C_{0.18})_4$) and $Fe_7C_3$. **b** Backscattered electron (BSE) image of sample PPMA#007.1 (same area as **a**) showing $Fe_7C_3$ carbide grains alongside diamond surrounded by Fe-nitride. **c** Sample PPMA#012; quench texture in the Fe–C–N system as a result of melting at 1400 °C. An experiment with the same starting mixture at 1000 °C (PPMA#013) was not molten and shows one homogenous phase. **d** PPMA#013 bright phase shows Fe-metal (6 at%N, 1.9 at%C) coexisting with darker $Fe_3C$ carbide. In contrast to experiment PPMA#012 (1400 °C), this sample shows big and homogenous crystals with straight grain boundaries and ~ 120° dihedral angles **e** Coexisting nitride and Fe-metal in experiment PPMA#015.1. **f** Experimental results of run PPMA15.2; carbide and nitride in equilibrium. **g** Coexisting $Fe_7C_3$ and $Fe_3C$. The two phases in sample SUS2.1 differ only slightly in gray scales in BSE images. The smaller and darker crystals are $Fe_7C_3$, the larger crystals are $Fe_3C$. **h** & **i** show $Fe_3C$ coexisting with ε-$Fe_3N$ or Fe–Ni metal

Siderazot ($Fe_3N_{1.33}$) or Roaldit ($Fe_4N$). In the ε-$Fe_xN$ structure, the Fe atoms are hexagonal close-packed and the N atoms occupy the octahedral sites of the Fe atomic framework. However, the occupation of the octahedral sites perpendicular to the c axis is variable; in the case of ε-$Fe_3N$, every third octahedral site is occupied by N, resulting in an increase in the volume of the unit cell (Jack 1952), creating more space for N atoms, which accounts for the large variability of N in the ε-$Fe_xN$ phase (see Fig. 3).

In agreement with structural studies (Ågren 1979; Frisk 1987; Göhring et al. 2016; Jack 1952; Stein et al. 2013) of the ε-$Fe_xN$ phase, our experimental results reveal a large variability of N in the ε-$Fe_3N$ Phase (Tab. 2) indicating that ε-$Fe_xN$ is also non-stoichiometric at high-pressure and high-temperature conditions. Experiments with coexisting diamond and ε-$Fe_3N$ show that the carbon solubility in the ε-$Fe_3N$ phase at these conditions is $6.47 \pm 0.4$ at% (Tab. 2). In contrast, nitrogen solubility in Fe-carbides is rather low, and therefore, N does not act as a significant alloying element. The solubility of nitrogen in $Fe_7C_3$ is $1.19 \pm 0.37$ at% (PPMA7.1) and $< 1$ at% in $Fe_3C$ (SUS2.1).

Experiments containing Fe-metal and ε-$Fe_3N$ in equilibrium were conducted either with or without Ni to investigate the influence of Ni on the respective phase stability fields. Increasing Ni content affected the Fe–N side of the ternary phase diagram by opening the two-phase field of Fe–Ni

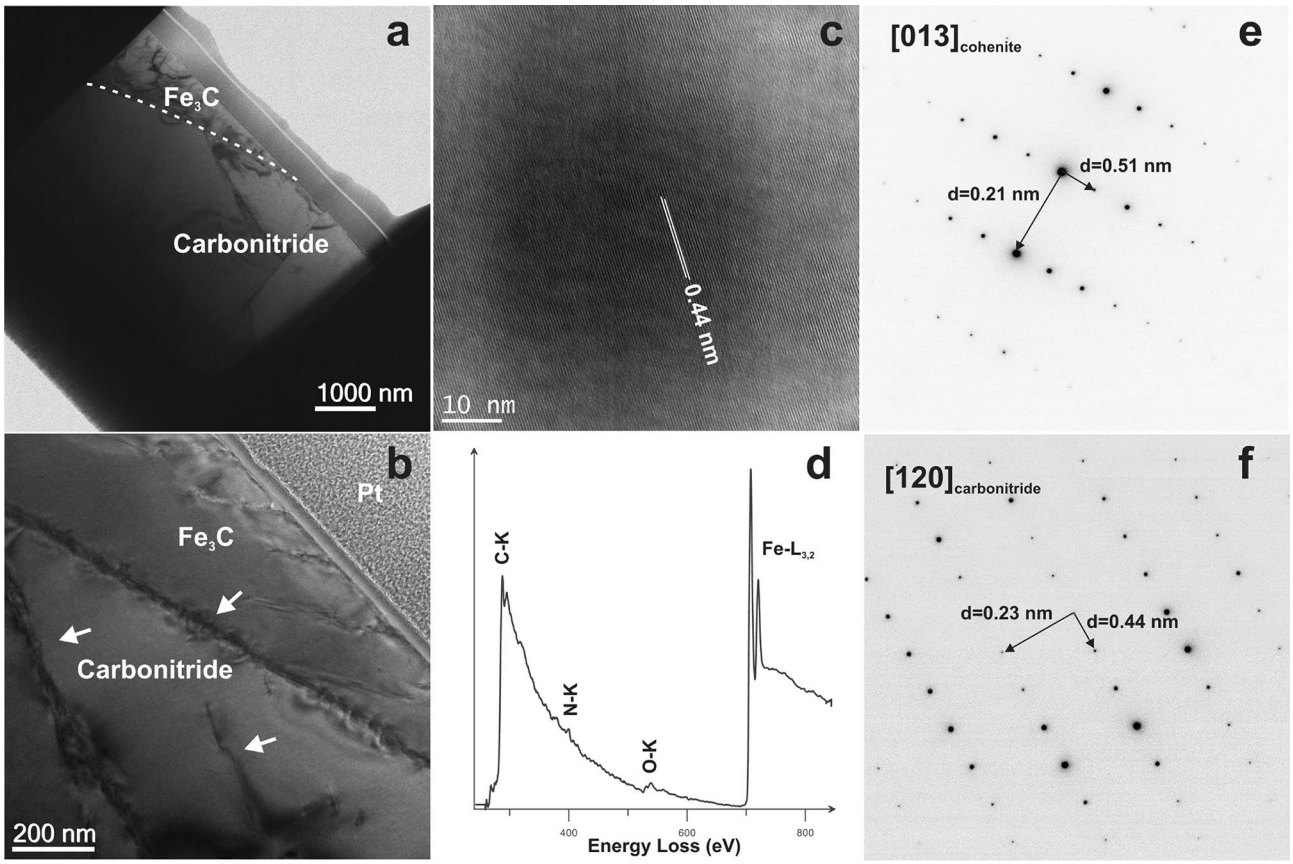


**Fig. 2** Results of TEM investigations. **a** Brightfield (BF) overview image of the FIB lamella. Coexisting phases in experiment PPMA15.1 consist of $Fe_3C$ (cohenite) and carbon-containing ε-$Fe_3N$ ("carbonitride"). **b** BF image of the boundary between the two phases showing abundant dislocations marked by arrows. **c** HR image of the carbonitride with (001) planes visible, disturbed by dislocations (darker areas). **d** EEL spectrum of the cohenite that could be quantified to stoichiometric $Fe_3C$ (deconvolved with the zero-loss peak to remove plural scattering, background-subtracted, and smoothed). Abundance of nitrogen is very low, detection of oxygen is likely due to secondary oxidation of the lamella. **e**, **f** indexed electron diffraction patterns of $Fe_3C$ and ε -$Fe_3N$

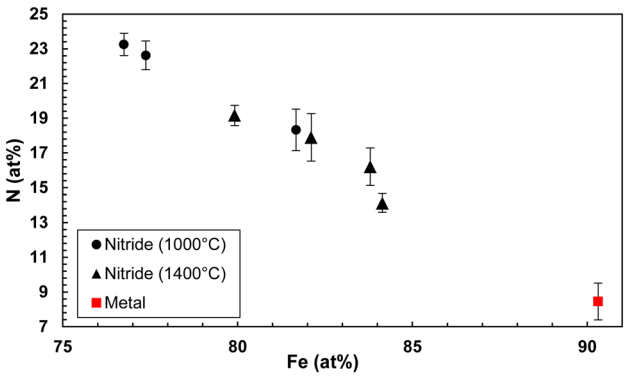


**Fig. 3** Nitrogen content of ε-$Fe_xN$ nitride as a function of Fe-content (at%). Light blue dots represent nitrides (< 2 at% C) from 1400 °C experiments, while dark blue squares are nitrides from 1000 °C runs. The red symbol shows Fe-metal which coexists with Fe-nitride in PPMA15.2 indicating the minimum N content in ε-Fe N at a concurrent maximum solubility of N in Fe-metal. Experiments in the Fe–N system follow a trend showing variable amounts of N in the ε-$Fe_3N$ phase

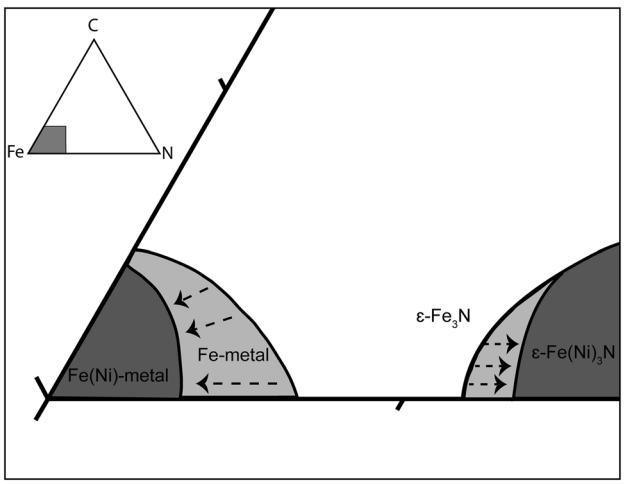


**Fig. 4** Fe–N side of the ternary phase diagram as shown in Fig. 5. Stability fields derived from Ni-free (light grey) and Ni-containing experiments (dark grey) indicate a change of shape and width of metal- and the ε-$Fe_3N$ stability fields with Ni

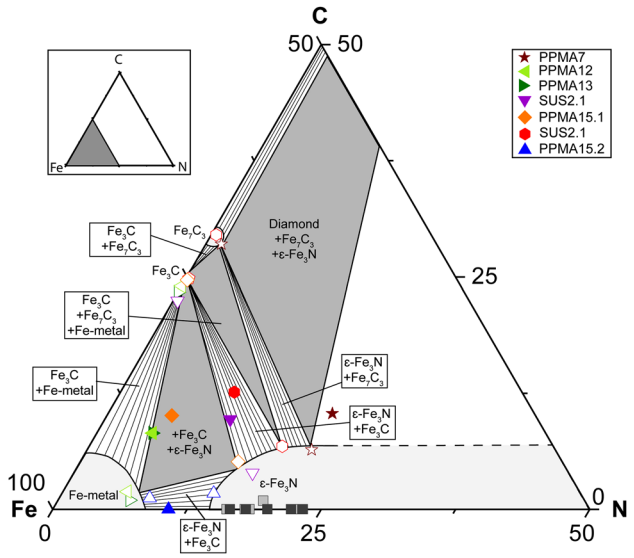


**Fig. 5** Ternary plot of the resulting Fe–C–N phases [at%] at 10 GPa and 1000 °C. Starting materials (filled) and related phases (unfilled) are the same color. Dark grey fields represent invariant assemblages, while white fields represent univariant assemblages. Tie lines in univariant fields reflect the compositional variability of the metal and the ε-$Fe_xN$ phase. Grey squares represent single-phase experiments in the ε-$Fe_xN$ stability field. As a result of Fe oxidation, N contents of resulting phases (unfilled symbols) are slightly higher than in the starting composition (filled symbols)

metal and ε-Fe(Ni)$_3$N (Fig. 4). Maximum N solubility in Fe-metal at 1000 °C and 10 GPa is ~ 8.4 ± 1 at% decreasing to ~ 3.6 ± 1 at% at high Ni-content (~ 27.4 at% Ni).

Therefore, increasing Ni results in smaller Fe-metal and ε-$Fe_3N$ stability fields with a larger two-phase field between ε-$Fe_3N$ and (Fe,Ni)-metal. In general, the effect that both increasing Ni and increasing C concentrations reduce the solubility of N in solid Fe metal is comparable to the behavior of these elements in molten systems (Jackson et al. 2021a; Grewal et al. 2021).

### Phase relations within the (Fe,Ni)–N–C ternary system

Based on the experimental results we constructed a ternary phase diagram (Fe–N–C) showing the stability fields of different phases at 1000 °C and 10 GPa. Stability fields were defined by connecting coexisting phases of the same experiment with tie-lines (e.g. metal–$Fe_3C$, metal–ε-$Fe_3N$, $Fe_3N$–$Fe_3C$–$Fe_7C_3$, $Fe_7C_3$–ε-$Fe_3N$–diamond).

On the Fe–C side of the diagram, Fe(Ni)-metal and $Fe_3C$ define a two-phase field with variable N contents in the metal and very low N concentrations in $Fe_3C$. Towards higher C contents in the Fe–C system, $Fe_7C_3$ forms, resulting in a two-phase field between $Fe_3C$ and $Fe_7C_3$. With increasing C concentration, $Fe_7C_3$ coexists with diamond. As N is added to the Fe–C binary, a three-phase field opens between Fe(Ni)-metal, $Fe_3C$, and C bearing ε-$Fe_3N$. The same applies to the $Fe_3C$–$Fe_7C_3$ and also $Fe_7C_3$–diamond stability fields with coexisting ε-$Fe_3N$ as the stable N-rich phase.

With increasing N in the Fe–N binary, ε-$Fe_3N$ is in equilibrium with Fe-metal defining a two-phase field, while higher N concentrations result in a single ε-$Fe_3N$ phase of varying stoichiometry (see Fig. 3), depending on N content of the bulk system. While most experiments define fixed edges of the ternary, experiments sharing an edge with the ε-$Fe_3N$ field, show variability of N and also C in ε-$Fe_3N$. As displayed by the stability fields of carbides, N solubility in $Fe_7C_3$ (~ 1,47 at% or ~ 0,48 wt%) is higher than in $Fe_3C$ (< 1 at%). The extremely low solubility of N (i.e., below the EPMA detection limit) in cohenite ($Fe_3C$) measured here agrees well with previous studies (Kruk et al. 2020, 2021). Nitrogen-containing Fe-metal coexisting with $Fe_3C$ (both quenched melt) indicates a maximum C solubility of 0.97 ± 0.35 at% in Ni-free experiment PPMA12 at 1400 °C [note that PPMA12 was molten and quench structures were measured as shown in Fig. 1c)], while it is 1.90 ± 0.95 at% in PPMA13 (1000 °C). In the N-free Fe–Ni system, the obtained maximum C in austenite (γ-Fe) is 3.99 ± 0.38 at%.

Because we did not conduct any N-free experiments, the stability field of Fe-metal was constructed by combining our data with results from Kruk et al. (2021), who reported 2,1–3,1 at% C in Fe-metal coexisting with $Fe_3C$ carbide (1350 °C and 7,8 GPa), and Rohrbach et al. (2014) who measured C solubility in Fe(Ni)-metal of ~ 5 at% indicating higher C solubility in Ni-rich metals compared to Ni-free compositions.

The ternary diagram (Fig. 5) depicts the starting material compositions (filled symbols) and resulting coexisting phases (unfilled symbols).

## Discussion

### C/N solubility and (Fe,Ni)–N–C melting temperatures

The melting behavior of Fe–N–C phases at mantle conditions largely controls the mobility as well as the storage conditions of crystalline Fe–C–N phases or melts in the mantle. Previous studies (Sokol et al. 2017a, b) show a large liquid field between $Fe_3C$, Fe-metal, and ε-$Fe_3N$ at 7.8 GPa and 1350 °C. Our experiments, were performed 10 GPa and 1000 °C contain no evidence of melting and reveal insights into the sub-solidus phase assemblages in the Fe–N–C system.. We have noticed melting only in 1400 °C experiments in the Fe–N–C system (Fig. 1c) while runs within the pure Fe–N systems contained exclusively solid phases. Fe–C melting temperatures at 10 GPa were determined

experimentally to be ~ 1210 °C, decreasing with increasing Ni content to ~ 1125 °C (Rohrbach et al. 2014). Melting in the (Fe,Ni)–N–C system, therefore, should begin slightly lower at around 1100 °C.

Although the size and location of stability fields in melt-containing experiments are in good agreement with our sub-solidus experimental runs, the C solubility in ε-$Fe_3N$ is slightly higher (~ 9.6 at%) at 7.8 GPa and 1150 °C (Kruk et al. 2021) compared to our experimental results at 1000 °C and 10 GPa (6.7 ± 0.7 at% C (SUS2.1) and 6.41 ± 0.76 C (PPMA7.1)). At 1 atm, ε-$Fe_3N$ can incorporate high amounts of C, replacing N atoms without changing the crystal structure. This results in the formation of high-C ε-$Fe_3N$ (Jack 1948) which is in good agreement with our findings in the Fe–N–C system at 10 GPa.

Nitrogen solubility in carbides is variable in $Fe_7C_3$ (up to 1.47 ± 0.30 at% N), while $Fe_3C$ does not contain any measurable N. $Fe_7C_3$ has also been proposed to be present in the mantle as an accessory phase (Dasgupta and Hirschmann 2010; Rohrbach et al. 2014) and as a possible C-host in the Earth's core (Liu et al. 2016a, 2016b).

## (Fe,Ni)–N–C inclusions in diamonds: comparison with experimental results

Nitrogen-free carbides in natural diamonds (Kaminsky and Wirth 2011) contain highly variable amounts of C as they follow compositional trends towards higher and lower C concentrations in between the experimentally determined Fe–C stability fields (Fig. 6). Fe–C phases other than $Fe_3C$ and $Fe_7C_3$ are not stable in any of our experiments or other experimental studies (Hirayama et al. 1993; Lord et al. 2009; Rohrbach et al. 2014; Tsuzuki et al. 1984; Wood 1993). The N solubility in carbides, especially in $Fe_3C$, as well as the C solubility in the ε-$Fe_3N$ phase, is very low at the P–T conditions of this study. Consequently, as shown in Fig. 6, the nitrocarbides with N contents up to several at% N, cannot be reproduced by our experiments but are well within the ternary stability field diamond–$Fe_7C_3$– ε $Fe_3N$. Similarly, several N-free non-stoichiometric Fe-carbides (Kaminsky and Wirth 2011) are also not stable at out experimental conditions but are located in-between the $Fe_3C$, $Fe_7C_3$ and diamond fields at 10 GPa and 1000 °C (Fig. 6). However, carbonitrides ($Fe_9(N_{0.8}C_{0.20})_4$), that have been found as diamond inclusions, Kaminsky and Wirth (2017) were stable in our experiments. Even though the natural inclusions contain slightly higher N concentrations than the experimentally synthesized ones (Tab.2), they are located on the edge of the constructed ε-$Fe_3N$ stability field (Fig. 6) supporting our finding of non-stoichiometric ε-$Fe_3N$. Stoichiometric nitrides $Fe_2N$ and $Fe_3N$ coexisting with ($Fe_9(N_{0.8}C_{0.20})_4$) in natural diamonds, were also not reproduced in our experiments.

Our experimental results indicate phase relations and phase compositions which, in some cases, do not match the compositions of natural inclusions, and we surmise that this could be caused by the fact that the P–T-range covered by our experiments is limited to upper mantle conditions. New experiments at higher pressure at lower-mantle or even core-mantle boundary conditions are needed to further constrain the source region of the diamond inclusion Fe(Ni)–N–C phases.

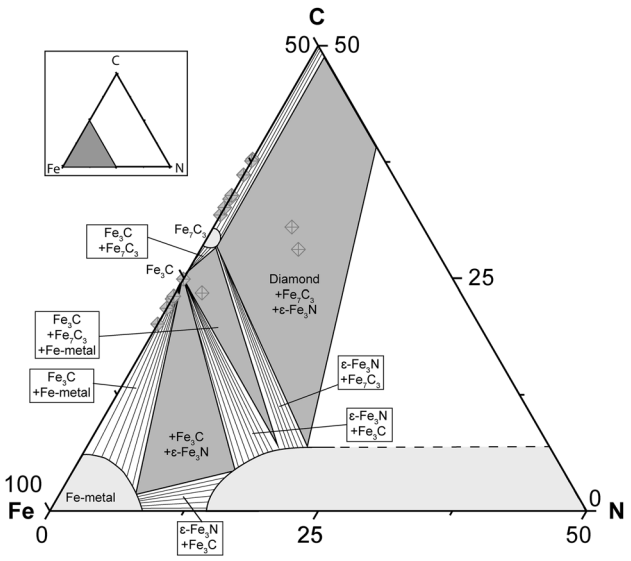


**Fig. 6** Schematic ternary diagram with natural diamond inclusions (grey diamonds) from (Kaminsky and Wirth 2011, 2017). Natural inclusions, such as high-N cohenite, and high-N $Fe_7C_3$ are located within the stability fields. $Fe_9(N_{0.8}C_{0.20})_4$ is located at the edge of the ε-$Fe_3N$ stability field

## Ni in (Fe,Ni)–N–C phases

Oxygen fugacity ($fO_2$) is a key factor controlling the stability of redox-sensitive mineral assemblages, including reduced phases, such as carbides (Dasgupta and Hirschmann 2010; Rohrbach et al. 2014). In the Earth's mantle, $fO_2$ is mainly controlled by the equilibrium between ferric and ferrous iron-bearing phases. As shown by experimental studies (Frost et al. 2004; Rohrbach et al. 2007), as well as by thermodynamic calculations related to natural samples (Woodland and Koch 2003; Yaxley et al. 2012), $fO_2$ in the mantle is likely to decrease with increasing depth relative to mineral buffer systems (Wood et al. 1990; O'Neill et al. 1993a; Ballhaus 1995; Frost and McCammon 2008). As a consequence, the deep upper mantle > 250 km is reduced enough to stabilize native (Fe,Ni)-metal with coexistent garnet peridotite (O'Neill et al. 1993b; Ballhaus 1995; Rohrbach et al. 2007, 2011). In our experiments, FeO coexists with (Fe,Ni) metal, nitrides, and carbides, confirming their stability near the

iron–wustite buffer (IW), and thus their stability in deeper regions of the Earth's mantle.

Our results show that all of our experimental Fe–N–C phases incorporate significant amounts of Ni; ε-$Fe_3N$ (up to 35.71 ± 0.60 at%), metal (54.06 ± 0.87 at%), and $Fe_3C$ (14.68 ± 0.75 at%). The metal phase, which is formed when $fO_2$ in the mantle intersects with the Ni precipitation curve, is expected to be Ni-rich ~ $Fe_{45}Ni_{55}$; (Frost and McCammon 2008; Rohrbach and Schmidt 2011). Thus, if Fe–N–C inclusions in diamond were formed in similarly primitive mantle regions or formed directly from these metals, i.e., through reaction with C and N rich fluids, we would expect such carbides and nitrides to be Ni-rich. However, the Ni contents in naturally occurring $Fe_3C$, $Fe_7C_3$, ε-$Fe_3N$, and oxide inclusions in diamonds from Rio Soriso region (Brazil) are generally very low, in a range of 0.35–0.93 at% (Kaminsky et al. 2015; Kaminsky and Wirth 2011, 2017). As the Fe–Ni ratio of the metal increases with depth to ~ $Fe_{90}Ni_{10}$ in the lower mantle (Frost and McCammon 2008), it seems, therefore, unlikely that the aforementioned inclusions formed in fertile or primitive peridotitic mantle regions. We rather suggest that the Ni-poor carbide, nitride, and carbonitride inclusions in diamonds (Kaminsky and Wirth 2011, 2017) originate in regions that are less primitive and consequently Ni-poor. A likely source region may be the crustal part of a deeply subducted plate, as Ni concentrations in metabasalts are rather low (81–137 ppm; e.g., Klein (2003). A subduction-related origin of the inclusions seems intuitive, since subduction of N-rich sediments and carbonates (Halama and Bebout 2021) enriches the source region of the diamonds (Smith and Kopylova 2014) in C and N. This would imply that the inclusions were trapped at rather low temperatures as the geothermal gradient within a subducted slab, especially on the top of the plate is suspected to be significantly lower than the normal mantle adiabat (Holt and Condit 2021; Peacock 2003). The subduction-related origin of the inclusions, therefore, seems intuitive, since N and C are transported into the mantle through subduction of N-rich sediments and carbonates (Halama and Bebout 2021), and this will enrich the source region of the diamonds in C and N (Smith and Kopylova 2014), to concentrations needed to stabilize diamond in the first place. Subduction zones could, therefore, be a possible formation regime of Fe–N–C phases with melting temperatures < 1400 °C and low Ni contents (see Fig. 7).

Considering the formation of (Fe,Ni)-nitrides and -carbides as a result of N and C subduction into the presumably metal-rich lowermost upper mantle (Frost et al. 2004) with thermal equilibration and melting, the question arises whether these melts can remain in the upper mantle or if they will move through the silicate mantle rock. Although experimentally synthesized Fe(Ni)–N–C phases melt at normal mantle adiabatic temperatures, some nitrides, carbides, and carbonitrides may remain in the upper mantle and reside in isolated colder mantle domains close to their region of formation. If one considers the large density contrasts between silicate mantle minerals or melts and Fe(Ni)-metal melts, molten Fe(Ni)–N–C should percolate deeper into the mantle, but only if these melts have wetting properties that allow them to move along grain boundaries.

Consequently, N and C storage in solid and/or liquid Fe–Ni metal may be important in the Earth's upper- and lower mantle. Yet, the vexing question remains whether

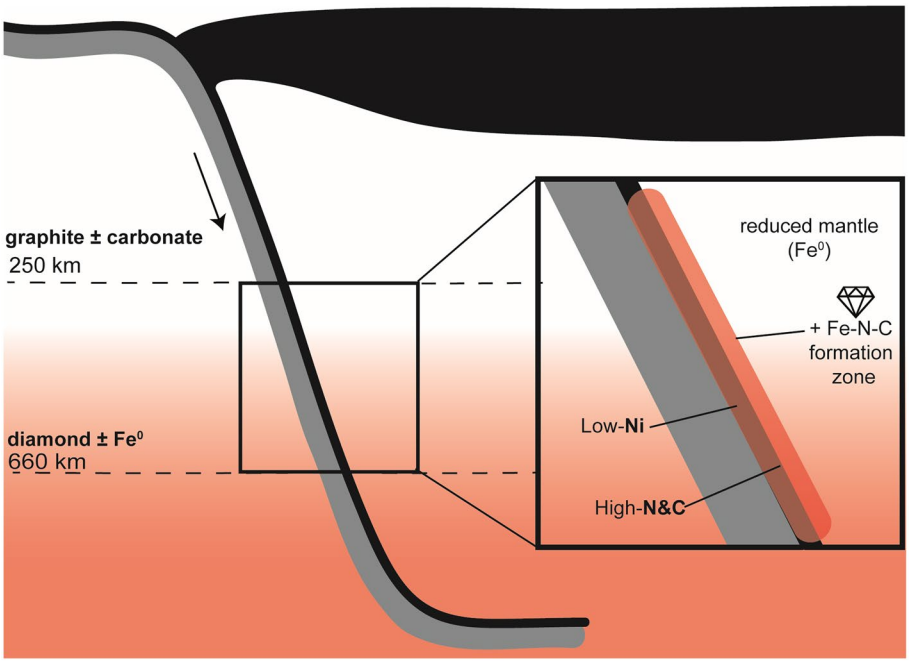


**Fig. 7** Schematically illustrated subduction zone. Nitrogen and C-rich sediments overlying low Ni metabasalts are subducted into the lowermost upper mantle (blue slab). Fe–N–C phases are formed at the slab–mantle interface (brown area) below 250 km depths, or when $fO_2$ is low enough to stabilize carbides. It is unclear what happens to the carbides and metallic Fe, as native Fe and diamond coexisting with may either melt and gravitationally sink into the lower mantle, they Fe–N–C phases may remain stable in cold isolated mantle domains or they may melt when heated to ambient mantle temperatures

the Fe-carbide phases are stored, or, if they melt and percolate through a partially molten lower mantle. Therefore, further investigation of Fe–N–C melt mobility in peridotitic rocks is critically needed to investigate the whereabouts of possible N- and C-rich metal melts in the mantle. Furthermore, experimental data on N (and also C) partitioning between Fe(Ni)–N–C solids or melts and transition zone and lower-mantle minerals are needed to constrain the deep geological N- and C-cycles accurately.

## Conclusions

- Experimentally determined phase relations in the system (Fe,Ni)–N–C provide insights into the stability of nitrides, carbides, and carbonitrides at lowermost upper-mantle conditions. The experimental results show that (N-rich) metal phases as well as Fe-nitrides and -carbides can be stable in the deep upper mantle and they can coexist with and diamond at sub-solidus conditions.
- When we compare the experimental results with natural diamond inclusions, our data indicates that the diamonds, that contain similar carbides and nitrides, were formed in subduction-related Ni-poor regions in the deep mantle. N-rich carbides, stoichiometric nitrides, and carbides with stoichiometries different to $Fe_3C$ and $Fe_7C_3$ were not part of the equilibrium subsolidus phase assemblage in our experiments and were consequently trapped by natural diamond at quite different P–T conditions.

**Supplementary Information** The online version contains supplementary material available at https://doi.org/10.1007/s00410-023-02084-y.

**Acknowledgements** Our thanks go to Beate Schmitte for her superb support during EPMA, Maik Trogisch for his excellent sample preparation, Peter Weitkamp, Christopher Fritzsche in the precision engineering workshops, and Ludger Buxtrup, Samuel Flunkert, and Andrew Hardes for support in all things electronics. We also acknowledge funding of the ThermoFisher TEM "Themis" by the DFG via the Major Research Instrumentation Program under INST 211/719-1. We thank B. Wood and an anonymous reviewer for thoughtful reviews that significantly improved our manuscript as well as D. Canil for constructive comments and efficient editorial handling.

**Author contributions** All authors have given approval to the final version of the manuscript.

**Funding** Open Access funding enabled and organized by Projekt DEAL. We acknowledge funding by the Deutsche Forschungsgemeinschaft (DFG)—Project-D 263649064—SFB TRR–170. This is SFB TRR 170 publication no 208.

Deutsche Forschungsgemeinschaft,Project-D 263649064—SFB TRR–170,INST 211/ 719-1.

**Data availability** The authors confirm that the data supporting the findings in this study are available within the article and the supplementary materials.

## Declarations

**Conflict of interest** The authors declare that there are no known conflicts of interest that have affected data acquisition or presented interpretations.



## References

Ågren J (1979) A thermodynamic analysis of the Fe−C and Fe−N phase diagrams. Metall and Mater Trans A 10:1847–1852. https://doi.org/10.1007/BF02811728

Aiuppa A, Casetta F, Coltorti M, Stagno V, Tamburello G (2021) Carbon concentration increases with depth of melting in Earth's upper mantle. Nat Geosci 14:697–703. https://doi.org/10.1038/s41561-021-00797-y

Armstrong JT (1991) Quantitative elemental analysis of individual microparticles with electron beam instruments. In: Heinrich KFJ, Newbury DE (eds) Electron probe quantitation. Springer Science+Business Media, New York, pp 261–315

Ashfold MNR, Goss JP, Green BL, May PW, Newton ME, Peaker CV (2020) Nitrogen in diamond. Chem Rev 120:5745–5794. https://doi.org/10.1021/acs.chemrev.9b00518

Ballhaus C (1995) Is the upper mantle metal-saturated? Earth Planet Sci Lett 132:75–86. https://doi.org/10.1016/0012-821X(95)00047-G

Bebout GE, Fogel ML, Cartigny P (2013) Nitrogen: highly volatile yet surprisingly compatible. Elements 9:333–338. https://doi.org/10.2113/gselements.9.5.333

Bulanova GP, Zayakina N (1991) graphite-iron-cohenite assemblage in the central zone of diamond from 23rd party Congress kimberlite. Dokl Akad Nauk SSSR 317:706–709

Dasgupta R (2013) Ingassing, storage, and outgassing of terrestrial carbon through geologic time. Rev Mineral Geochem 75:183–229. https://doi.org/10.2138/rmg.2013.75.7

Dasgupta R, Hirschmann MM (2010) The deep carbon cycle and melting in Earth's interior. Earth Planet Sci Lett 298:1–13. https://doi.org/10.1016/j.epsl.2010.06.039

Dasgupta R, Walker D (2008) Carbon solubility in core melts in a shallow magma ocean environment and distribution of carbon between the Earth's core and the mantle. Geochim Cosmochim Acta 72:4627–4641. https://doi.org/10.1016/j.gca.2008.06.023

Ertl G, Huber M, Thiele N (1979) Formation and decomposition of nitrides on iron surfaces. Zeitschrift Für Naturforschung A 34:30–39. https://doi.org/10.1515/zna-1979-0106

Fischer RA, Cottrell E, Hauri E, Lee KKM, Le Voyer M (2020) The carbon content of Earth and its core. Proc Natl Acad Sci USA 117:8743–8749. https://doi.org/10.1073/pnas.1919930117

Flemetakis S, Berndt J, Klemme S, Genske F, Cadoux A, Louvel M, Rohrbach A (2020) An Improved Electron Microprobe Method for the Analysis of Halogens in Natural Silicate Glasses. Microsc Microanal 26:857–866. https://doi.org/10.1017/S1431927620013495

Frisk K (1987) A new assessment of the Fe-N phase diagram. Calphad 11:127–134. https://doi.org/10.1016/0364-5916(87)90004-6

Frost DJ, McCammon CA (2008) The redox state of earth's mantle. Annu Rev Earth Planet Sci 36:389–420. https://doi.org/10.1146/annurev.earth.36.031207.124322

Frost DJ, Liebske C, Langenhorst F, McCammon CA, Trønnes RG, Rubie DC (2004) Experimental evidence for the existence of iron-rich metal in the Earth's lower mantle. Nature 428:409–412. https://doi.org/10.1038/nature02413

Fukuyama K, Kagi H, Inoue T, Kakizawa S, Shinmei T, Sano Y, Deligny C, Füri E (2023) Temperature dependence of nitrogen solubility in bridgmanite and evolution of nitrogen storage capacity in the lower mantle. Sci Rep 13:3537. https://doi.org/10.1038/s41598-023-30556-5

Göhring H, Fabrichnaya O, Leineweber A, Mittemeijer EJ (2016) Thermodynamics of the Fe-N and Fe-N-C systems: the Fe-N and Fe-N-C phase diagrams revisited. Metall Mater Trans A 47:6173–6186. https://doi.org/10.1007/s11661-016-3731-0

Goldblatt C, Claire MW, Lenton TM, Matthews AJ, Watson AJ, Zahnle KJ (2009) Nitrogen-enhanced greenhouse warming on early Earth. Nat Geosci 2:891–896. https://doi.org/10.1038/ngeo692

Grewal DS, Dasgupta R, Hough T, Farnell A (2021) Rates of protoplanetary accretion and differentiation set nitrogen budget of rocky planets. Nat Geosci 14:369–376. https://doi.org/10.1038/s41561-021-00733-0

Halama R, Bebout G (2021) Earth's nitrogen and carbon cycles. Sp Sci Rev. https://doi.org/10.1007/s11214-021-00826-7

Halama R, Bebout GE, John T, Scambelluri M (2014) Nitrogen recycling in subducted mantle rocks and implications for the global nitrogen cycle. Int J Earth Sci 103:2081–2099. https://doi.org/10.1007/s00531-012-0782-3

Hirayama Y, Fujii T, Kurita K (1993) The melting relation of the system, iron and carbon at high pressure and its bearing on the early stage of the Earth. Geophys Res Lett 20:2095–2098. https://doi.org/10.1029/93GL02131

Hirschmann MM (2018) Comparative deep Earth volatile cycles: the case for C recycling from exosphere/mantle fractionation of major (H2O, C, N) volatiles and from H2O/Ce, CO2/Ba, and CO2/Nb exosphere ratios. Earth Planet Sci Lett 502:262–273. https://doi.org/10.1016/j.epsl.2018.08.023

Holt AF, Condit CB (2021) Slab temperature evolution over the lifetime of a subduction zone. Geochem Geophys Geosyst. https://doi.org/10.1029/2020GC009476

Jack KH (1948) Binary and ternary interstitial alloys-II. The iron-carbon-nitrogen system. Proc R Soc Lond Ser A Math Phys Sci 195:41–55. https://doi.org/10.1098/rspa.1948.0101

Jack KH (1952) The iron–nitrogen system: the crystal structures of ε-phase iron nitrides. Acta Crystallogr A 5:404–411. https://doi.org/10.1107/S0365110X52001258

Jackson C, Cottrell E, Du Z, Bennett NR, Fei Y (2021a) High pressure redistribution of nitrogen and sulfur during planetary stratification. Geochem Persp Lett. https://doi.org/10.7185/geochemlet.2122

Jackson CR, Cottrell E, Andrews B (2021b) Warm and oxidizing slabs limit ingassing efficiency of nitrogen to the mantle. Earth Planet Sci Lett 553:116615. https://doi.org/10.1016/j.epsl.2020.116615

Javoy M, Pineau F (1991) The volatiles record of a "popping" rock from the Mid-Atlantic Ridge at 14°N: chemical and isotopic composition of gas trapped in the vesicles. Earth Planet Sci Lett 107:598–611. https://doi.org/10.1016/0012-821X(91)90104-P

Johnson B, Goldblatt C (2015) The nitrogen budget of earth. Earth Sci Rev 148:150–173. https://doi.org/10.1016/j.earscirev.2015.05.006

Kaminsky F, Wirth R (2011) Iron carbide inclusions in lower-mantle diamond from Juina, Brazil. Can Mineral 49:555–572. https://doi.org/10.3749/canmin.49.2.555

Kaminsky F, Wirth R (2017) Nitrides and carbonitrides from the lowermost mantle and their importance in the search for Earth's "lost" nitrogen. Am Miner 102:1667–1676. https://doi.org/10.2138/am-2017-6101

Kaminsky F, Wirth R, Schreiber A (2015) A microinclusion of lower-mantle rock and other minerals and nitrogen lower-mantle inclusions in a diamond. Can Mineral 53:83–104. https://doi.org/10.3749/canmin.1400070

Keppler H, Wiedenbeck M, Shcheka SS (2003) Carbon solubility in olivine and the mode of carbon storage in the Earth's mantle. Nature 424:414–416. https://doi.org/10.1038/nature01828

Keppler H, Cialdella L, Couffignal F, Wiedenbeck M (2022) The solubility of N2 in silicate melts and nitrogen partitioning between upper mantle minerals and basalt. Contrib Mineral Petrol. https://doi.org/10.1007/s00410-022-01948-z

Klein EM (2003) Geochemistry of the igneous oceanic crust. In: Treatise on geochemistry. Elsevier, pp 433–463. https://doi.org/10.1016/B0-08-043751-6/03030-9

Kruk AN, Sokol AG, Seryotkin YV, Palyanov YN (2020) Phase relations in the FeO-Fe3C-Fe3N System at 7.8 GPa and 1350 °C: implications for oxidation of native iron at 250 km. Minerals 10:984. https://doi.org/10.3390/min10110984

Kruk AN, Korablin AA, Sokol AG, Palyanov YN (2021) Phase relations in the Fe-Fe 3 C-Fe 3 N system at 7.8 GPa and 1150°C: implications for C and N hosts in metal-saturated mantle. High Press Res 41:392–404. https://doi.org/10.1080/08957959.2021.1998479

Kurz W, Fisher DJ (1998) Fundamentals of solidification, 4th edn. Trans Tech Publications, Uetikon-Zuerich

Leineweber A, Jacobs H, Hüning F, Lueken H, Kockelmann W (2001) Nitrogen ordering and ferromagnetic properties of ϵ-Fe3N1+x (0.10≤x≤0.39) and ϵ-Fe3(N0.80C0.20)1.38. J Alloy Compd 316:21–38. https://doi.org/10.1016/S0925-8388(00)01435-3

Li Y, Marty B, Shcheka S, Zimmermann L, Keppler H (2016) Nitrogen isotope fractionation during terrestrial core-mantle separation. Geochem Perspect Lett. https://doi.org/10.7185/geochemlet.1614

Liu J, Li J, Ikuta D (2016a) Elastic softening in Fe 7 C 3 with implications for Earth's deep carbon reservoirs. J Geophys Res Solid Earth 121:1514–1524. https://doi.org/10.1002/2015JB012701

Liu J, Lin J-F, Prakapenka VB, Prescher C, Yoshino T (2016b) Phase relations of Fe 3 C and Fe 7 C 3 up to 185 GPa and 5200 K: Implication for the stability of iron carbide in the Earth's core. Geophys Res Lett 43:12415–12422. https://doi.org/10.1002/2016GL071353

Lord OT, Walter MJ, Dasgupta R, Walker D, Clark SM (2009) Melting in the Fe–C system to 70 GPa. Earth Planet Sci Lett 284:157–167. https://doi.org/10.1016/j.epsl.2009.04.017

Marty B (2012) The origins and concentrations of water, carbon, nitrogen and noble gases on Earth. Earth Planet Sci Lett 313–314:56–66. https://doi.org/10.1016/j.epsl.2011.10.040

Marty B, Tolstikhin IN (1998) CO2 fluxes from mid-ocean ridges, arcs and plumes. Chem Geol 145:233–248. https://doi.org/10.1016/S0009-2541(97)00145-9

Marty B, Almayrac M, Barry PH, Bekaert DV, Broadley MW, Byrne DJ, Ballentine CJ, Caracausi A (2020) An evaluation of the C/N ratio of the mantle from natural CO2-rich gas analysis:

geochemical and cosmochemical implications. Earth Planet Sci Lett 551:116574. https://doi.org/10.1016/j.epsl.2020.116574
McDonough WF, Sun S (1995) The composition of the Earth. Chem Geol 120:223–253. https://doi.org/10.1016/0009-2541(94)00140-4
Mikhail S, Howell D (2016) A petrological assessment of diamond as a recorder of the mantle nitrogen cycle. Am Miner 101:780–787. https://doi.org/10.2138/am-2016-5464
Ni H, Keppler H (2013) Carbon in silicate melts. Rev Mineral Geochem 75:251–287. https://doi.org/10.2138/rmg.2013.75.9
O'Neill HS, McCammon CA, Canil D, Rubie DC, Ross CR, Seifert F (1993b) Mössbauer spectroscopy of mantle transition zone phases and determination of minimum Fe3+ content. Am Miner 78:456–460
O'Neill HS, Rubie DC, Canil D, Geiger CA, Ross CR, Seifert F, Woodland AB (1993a) Ferric iron in the upper mantle and in transition zone assemblages: implications for relative oxygen fugacities in the mantle, pp 73–88. https://doi.org/10.1029/GM074p0073
Palya AP, Buick IS, Bebout GE (2011) Storage and mobility of nitrogen in the continental crust: evidence from partially melted metasedimentary rocks, Mt. Stafford, Australia. Chem Geol 281:211–226. https://doi.org/10.1016/j.chemgeo.2010.12.009
Peacock SM (2003) Thermal structure and metamorphic evolution of subducting slabs. In: Eiler J (ed) Inside the subduction factory, vol 138. American Geophysical Union, Washington D. C., pp 7–22
Rohrbach A, Schmidt MW (2011) Redox freezing and melting in the Earth's deep mantle resulting from carbon-iron redox coupling. Nature 472:209–212. https://doi.org/10.1038/nature09899
Rohrbach A, Ballhaus C, Golla-Schindler U, Ulmer P, Kamenetsky VS, Kuzmin DV (2007) Metal saturation in the upper mantle. Nature 449:456–458. https://doi.org/10.1038/nature06183
Rohrbach A, Ballhaus C, Ulmer P, Golla-Schindler U, Schönbohm D (2011) Experimental evidence for a reduced metal-saturated upper mantle. J Petrol 52:717–731. https://doi.org/10.1093/petrology/egq101
Rohrbach A, Ghosh S, Schmidt MW, Wijbrans CH, Klemme S (2014) The stability of Fe–Ni carbides in the Earth's mantle: Evidence for a low Fe–Ni–C melt fraction in the deep mantle. Earth Planet Sci Lett 388:211–221. https://doi.org/10.1016/j.epsl.2013.12.007
Rubie DC (1999) Characterising the sample environment in multianvil high-pressure experiments. Phase Transit 68:431–451. https://doi.org/10.1080/01411599908224526
Saal AE, Hauri EH, Langmuir CH, Perfit MR (2002) Vapour undersaturation in primitive mid-ocean-ridge basalt and the volatile content of Earth's upper mantle. Nature 419:451–455. https://doi.org/10.1038/nature01073
Sano Y, Takahata N, Nishio Y, Fischer TP, Williams SN (2001) Volcanic flux of nitrogen from the Earth. Chem Geol 171:263–271. https://doi.org/10.1016/S0009-2541(00)00252-7
Shcheka SS, Wiedenbeck M, Frost DJ, Keppler H (2006) Carbon solubility in mantle minerals. Earth Planet Sci Lett 245:730–742. https://doi.org/10.1016/j.epsl.2006.03.036
Smith EM, Kopylova MG (2014) Implications of metallic iron for diamonds and nitrogen in the sublithospheric mantle. Can J Earth Sci 51:510–516. https://doi.org/10.1139/cjes-2013-0218
Sokol AG, Kruk AN, Seryotkin YV, Korablin AA, Palyanov YN (2017a) Phase relations in the Fe-Fe 3 C-Fe 3 N system at 7.8 GPa and 1350 °C: implications for carbon and nitrogen hosts in Fe 0 -saturated upper mantle. Phys Earth Planet Inter 265:43–53. https://doi.org/10.1016/j.pepi.2017.02.007
Sokol AG, Kruk AN, Palyanov YN, Sobolev NV (2017b) Phases of the Fe–C–N system as hosts of mantle carbon and nitrogen: experimental studies at 7.8 GPa and 1350°C. Dokl Earth Sci 475:780–783. https://doi.org/10.1134/S1028334X17070091
Stagno V, Ojwang DO, McCammon CA, Frost DJ (2013) The oxidation state of the mantle and the extraction of carbon from Earth's interior. Nature 493:84–88. https://doi.org/10.1038/nature11679
Stein J, Schacherl RE, Jung M, Meka S, Rheingans B, Mittemeijer EJ (2013) Solubility of nitrogen in ferrite; the Fe–N phase diagram. Int J Mater Res 104:1053–1065. https://doi.org/10.3139/146.110968
Trull T, Nadeau S, Pineau F, Polve´Javoy MM (1993) C-He systematics in hotspot xenoliths: Implications for mantle carbon contents and carbon recycling. Earth Planet Sci Lett 118:43–64. https://doi.org/10.1016/0012-821X(93)90158-6
Tsuzuki A, Sago S, Hirano S-I, Naka S (1984) High temperature and pressure preparation and properties of iron carbides Fe7C3 and Fe3C. J Mater Sci 19:2513–2518. https://doi.org/10.1007/BF00550805
Weidner A, Biermann H (2015) Case studies on the application of high-resolution electron channelling contrast imaging—investigation of defects and defect arrangements in metallic materials. Phil Mag 95:759–793. https://doi.org/10.1080/14786435.2015.1006296
White WM (2013) Geochemistry. Wiley-Blackwell, Oxford
Wijbrans CH, Rohrbach A, Klemme S (2016) An experimental investigation of the stability of majoritic garnet in the Earth's mantle and an improved majorite geobarometer. Contrib Mineral Petrol. https://doi.org/10.1007/s00410-016-1255-7
Wood BJ (1993) Carbon in the core. Earth Planet Sci Lett 117:593–607. https://doi.org/10.1016/0012-821X(93)90105-I
Wood BJ, Bryndzia LT, Johnson KE (1990) Mantle oxidation state and its relationship to tectonic environment and fluid speciation. Science 248:337–345. https://doi.org/10.1126/science.248.4953.337
Woodland A, Koch M (2003) Variation in oxygen fugacity with depth in the upper mantle beneath the Kaapvaal craton, Southern Africa. Earth Planet Sci Lett 214:295–310. https://doi.org/10.1016/S0012-821X(03)00379-0
Yang Y, Huang W, Qi Z, Xia Q (2022) Nitrogen retention in feldspar: implications for nitrogen transport in subduction zones. J Geophys Res Solid Earth 127:10. https://doi.org/10.1029/2021JB023347
Yaxley GM, Berry AJ, Kamenetsky VS, Woodland AB, Golovin AV (2012) An oxygen fugacity profile through the Siberian Craton—Fe K-edge XANES determinations of Fe3+/∑Fe in garnets in peridotite xenoliths from the Udachnaya East kimberlite. Lithos 140–141:142–151. https://doi.org/10.1016/j.lithos.2012.01.016
Yokochi R, Marty B, Chazot G, Burnard P (2009) Nitrogen in peridotite xenoliths: lithophile behavior and magmatic isotope fractionation. Geochim Cosmochim Acta 73:4843–4861. https://doi.org/10.1016/j.gca.2009.05.054
Yoshioka T, Wiedenbeck M, Shcheka S, Keppler H (2018) Nitrogen solubility in the deep mantle and the origin of Earth's primordial nitrogen budget. Earth Planet Sci Lett 488:134–143. https://doi.org/10.1016/j.epsl.2018.02.021
Zhang Y, Zindler A (1993) Distribution and evolution of carbon and nitrogen in Earth. Earth Planet Sci Lett 117:331–345. https://doi.org/10.1016/0012-821X(93)90088-Q